

## A REAL-TIME METHOD FOR VENTILATION AND BLOOD PULSATILITY SEPARATION IN FUNCTIONAL IMAGES OF THE CHEST

FERNANDO SILVA DE MOURA <sup>1</sup>, EDUARDO LEITE VIEIRA COSTA <sup>2</sup>  
AND MARCELO BRITTO PASSOS AMATO 

<sup>1</sup>Engineering, modelling and Applied Social Sciences Center, Federal University of ABC, Brazil

<sup>2</sup>Respiratory Intensive Care Unit, School of Medicine, University of São Paulo, Brazil

(Communicated by Malena Espanol)

**ABSTRACT.** Mapping the ventilation and the regional blood pulsatility behavior of the lung is essential for treating patients with respiratory failure, especially those under mechanical ventilation. The separation of ventilation and blood pulsatility in Electrical Impedance Tomography images of the thorax is the focus of this paper, with potential applications in medical imaging and other tomographic imaging modalities. The method has two stages. In the first stage, the algorithm is trained to identify the dynamic models of ventilation and pulsatility cycles separately. The second stage uses the adjusted models to separate new incoming images in real-time. During the training stage, two average cycles are estimated - one for ventilation and the other for blood pulsatility. Coherent averages of a training set of images are computed using triggering signals to identify the cycles. These average cycles are then used to adjust evolution models for real-time processing in the second stage. The proposed method was evaluated with experimental data in swines under mechanical ventilation. The robustness of the method against substantial changes in ventilation modes was assessed. The results show that the method was successful in separating ventilation and pulsatility, with only a small residual mixture, and showed that the method is robust.

**1. Introduction.** Mapping the ventilation and the regional functional behavior of the lung is of specific interest to clinicians treating patients with respiratory failure, especially those under mechanical ventilation. However, from a physiological point of view, the knowledge of the magnitude and distribution of lung ventilation is not sufficient as a sole criterion for the adjustment settings because of the importance of heart-lung interactions and their consequences in the hemodynamic profile of patients. For example, ventilation pressures that are optimal for the lung condition sometimes have to be lowered to avoid hemodynamic instability.

The heart and lungs function in series: all blood entering the right ventricle flows to the lungs for oxygenation, then to the left heart, and subsequently to the systemic circulation. Additionally, the heart and lungs share the same confined

2020 *Mathematics Subject Classification.* 92C50, 92C55.

*Key words and phrases.* Functional images, image separation, ventilation, blood pulsatility, tomography, principal component analysis, evolution model.

FSM thanks the financial support of São Paulo Research Foundation–FAPESP (2019/09154-7).

\*Corresponding author: Fernando Silva de Moura.

space within the chest cavity, competing for volume. Consequently, changes in intrathoracic pressures can significantly affect the hemodynamic interplay between the heart and lungs. Therefore, there are substantial differences in the heart-lung interactions according to the ventilatory condition. During inspiration in spontaneous ventilation, pleural pressures decrease due to the action of the respiratory muscles. Consequently, the pressure gradient from outside the chest wall favors venous return, leading to an increase in right ventricular preload. The left ventricle afterload, however, increases because the negative pleural pressure swing around the heart increases its transmural pressure. As a consequence, during the inspiration, there is an immediate reduction in the systemic stroke volume. After a few heartbeats, the increased venous return to the right ventricle hits the left ventricle, leading to a delayed increment in systemic stroke volume usually during the expiration phase. Conversely, during positive pressure ventilation, the right ventricle experiences a decrease in preload during the inspiratory phase due to an unfavorable venous pressure gradient. Additionally, the compression of the pulmonary vasculature increases right ventricular afterload. In contrast, the left ventricle is compressed by the elevated pleural pressure, which favors its ejection and reduces afterload. Similarly, the compression of the pulmonary circulation increases left ventricular preload. So if we analyze the cyclic alterations in the arterial pressure, we will perceive this physiological phenomenon known as reverse paradox pulse. There is a great interest in the study of this phenomenon as well as the heart-lung interactions. In the last two decades, several studies have demonstrated that analyzing cyclic changes in the arterial pressure curve can be used to evaluate the hemodynamic conditions of critically ill patients, particularly to assess whether they require additional volume infusion such as crystalloid solutions.

Electrical Impedance tomography (EIT) is a noninvasive, ionizing radiation-free monitoring tool that allows imaging of the ventilation and of systolic-related changes in blood volume (hereinafter referred to as *pulsatility*) [3]. However, it is difficult to image these cardiac-related changes because of the high amplitude of the ventilation component combined with the low amplitude of cardiac-related impedance changes and the known anatomical distortion of EIT scans. Several methods have been used to separate the ventilation and pulsatility components of the raw signal acquired by EIT. The simplest method is to perform a breath hold to remove respiratory changes, which also removes the ability to assess heart-lungs interactions [5]. Alternatively, electrocardiography-gating and frequency filtering have been suggested, which allow the acquisition of pulsatility components of EIT signal without respiratory interference [17, 18].

Other methods have been studied, among the methods we mention: evaluating lung pulsatility in mechanically ventilated patients using a band pass filtering technique and linear regression fit to establish regions of interest (ROI) [6]; using EIT images and calculating a  $V/Q$  ratio on experimental study with piglets [5]; estimating regional lung pulsatility based on first-pass kinetics of a bolus of hypertonic saline contrast [1]; and combining filtering and principal components analysis [4]. Among all these techniques, only the latter has the advantage of allowing real-time heart-lung interaction monitoring.

In this paper, the focus is the separation of ventilation and blood pulsatility in EIT images of the thorax. In the next sections, terms related to ventilation and pulsatility are employed. However, it is important to emphasize that the proposed

method can be promptly employed to separate other phenomena in medical imaging and other tomographic imaging modalities.

**2. Method description.** The method is divided in two stages: In the first part, the algorithm is trained to identify the dynamic models of ventilation and pulsatility cycles separately, while the second stage uses the adjusted models to separate new incoming images in real-time.

The training stage estimates two average cycles, one for ventilation and the other for blood pulsatility. It employs coherent averages of a training set of images obtained from the patient during a given period. The coherent averages are computed using triggering signals to identify the cycles, e.g., ECG signal for pulsatility cycles and peak pressure of the airways or flow signals for ventilation cycles. There are other possibilities. The average cycles are then used to adjust evolution models for the second stage when data is processed in real-time.

For the following sections, let each tomographic image be represented in flattened vector form by  $\mathbf{I} \in \mathbb{R}^\ell$  where  $\ell$  is the number of pixels of the image. Let a sequence of  $L$  images be represented by the ordered set  $\mathcal{S} = \{\mathbf{I}_1, \mathbf{I}_2, \dots, \mathbf{I}_L\} = \{\mathbf{I}_k\}_1^L$ . Also, let  $t_k = kT_s$  represent the time instant when the  $k$ -th image is acquired, where  $T_s = f_s^{-1}$  is the sampling period and  $f_s$  is the sampling frequency. Given analogous entities for ventilation  $x_v$  and pulsatility  $x_p$ , the notation  $x_{v,p}$  is used to mention them collectively. Finally,  $f_k$  and  $f[k]$  are two ways to represent a discrete-time function, sampled at  $t_k$ .

The proposed method allows these images to be the entire image  $\mathbf{I}_k$  or a subimage, resulting from region of interest (ROI) delimitation. By using subimages, the method must deal with smaller vectors, reducing the computational burden in both stages. One possible strategy is to remove regions of the image that do not play any role in ventilation/pulsatility via image segmentation. In the next sections the method is presented for the entire image  $\mathbf{I}_k$ ; changing the equations for subimages is a trivial task.

**2.1. Training stage.** The training stage requires a sequence of images of the patient under monitoring. No changes in ventilation modes should be performed during this stage if the patient is under mechanical ventilation, e.g. PEEP (positive end-expiratory pressure) titration, cycle randomization, and other recruitment maneuvers. It is also advisable to avoid moving or manipulating the patient during this period. Minimizing spurious movements and perturbations results in a set of images that represents more closely the dynamics of the ventilation and blood pulsatility.

**2.1.1. Decomposing the training set into pulsatility and ventilation cycles.** Let  $\mathcal{S}_T = \{\mathbf{I}_k\}_1^L$  be the ordered set of images for training. The first step is to identify ventilation and pulsatility cycles within  $\mathcal{S}_T$ . For this purpose, let  $p_v^+[k]$  be a discrete-time train of pulses acting as a trigger signal for the time instants when the volume of air in the lungs is maximum in each ventilation cycle. They mark the start of the expiratory phase in each cycle. The maxima instants can be identified from (i) ventilator sensors if such information is available, (ii) other measuring devices, e.g., esophageal catheter balloon, or (iii) approximately obtained from the training set, identifying the periodicity of one or more pixels known to pertain to the lung region. The method showed to be robust to small errors in  $p_v^+$ , so an approximation for it showed to produce satisfactory results.

Analogously, let  $p_v^-[k]$  be a trigger signal for the time instants when the air volume in the lungs is minimum in each ventilation cycle. They mark the start of the inspiratory phase in each cycle. Figure 1 presents representative ventilation cycles with associated  $p_v^\pm$  signals. Finally, let  $p_p[k]$  be a trigger signal for the time instants of the R wave peak of the ECG signal.

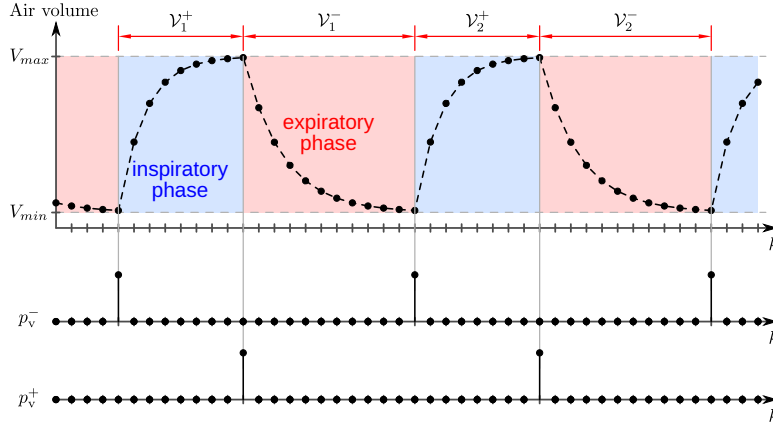


FIGURE 1. Representative pulmonary air volume signal as a function of discrete time  $k$  and associated train of pulses  $p_v^\pm$ .

Starting with the pulsatility, a set  $P_T = \{\mathcal{P}_i\}_1^{N_p}$  can be built where each element  $\mathcal{P}_i = \{\mathbf{I}_k\}_1^{L_i^p}$  is a subsequence of images extracted from  $\mathcal{S}_T$  comprised between two subsequent pulses of  $p_p$ , therefore each element  $\mathcal{P}_i$  is a sequence of images of a single pulsatility cycle. In this definition,  $L_i^p$  denotes the number of images in each subsequence  $\mathcal{P}_i$  and  $N_p$  is the number of complete pulsatility cycles extracted from the training set  $\mathcal{S}_T$ . The cycles  $\mathcal{P}_i$  do not have the same number of images since the heart rate is certain to vary during the training period among other reasons to be presented in the next section.

Now for the ventilation, two sets  $V_T^\pm = \{\mathcal{V}_i^\pm\}_1^{N_v^\pm}$  can be built. The elements  $\mathcal{V}_i^+ = \{\mathbf{I}_k\}_1^{L_i^{v+}}$  are subsequences of images extracted from  $\mathcal{S}_T$ , comprised between a pulse of  $p_v^-$  and the subsequent  $p_v^+$ , whilst the elements  $\mathcal{V}_i^- = \{\mathbf{I}_k\}_1^{L_i^{v-}}$  are subsequences of images extracted from  $\mathcal{S}_T$ , comprised between a pulse of  $p_v^+$  and the subsequent  $p_v^-$ . Thus, the elements  $\mathcal{V}_i^\pm$  are sequences of images of the inspiratory (+) and expiratory (-) phases of the ventilation cycle. In these sequences  $L_i^{\pm v}$  are the number of images in each subsequence, and  $N_v^\pm$  are the numbers of inspiratory and expiratory cycles within  $\mathcal{S}_T$ . Figure 1 shows the time intervals from which the subsequences  $\mathcal{V}_i^\pm$  are extracted. The rationale behind the partition of the ventilatory cycles into  $V_T^\pm$  will be made clear in the following section.

In the following subsections, the sets  $P_T$  and  $V_T^\pm$  are treated similarly. For this reason, they will be generally denoted by  $C_T = \{\mathcal{C}_i\}_1^{N_c}$  whose elements are  $\mathcal{C}_i = \{\mathbf{I}_k\}_1^{L_i^c}$ . Any specific operations for  $P_T$  and  $V_T^\pm$  will be explicitly mentioned.

**2.1.2. Average cycles.** The lengths  $L_i^c$  of the cycles  $\mathcal{C}_i$  are in general different due to natural variations, or due to errors in  $p_p$  and  $p_v^\pm$ . The main sources of errors in the triggering signals are small variations due to the sampling process and large

variations due to (i) faulty R wave detection, (ii) premature atrial contractions (PAC), (iii) premature ventricular contractions (PVC), or (iv) assisted ventilation modes that allow spontaneous breathing events like pressure support ventilation (PSV) [2, 16].

Due to the variations in  $L_i^c$ , it is necessary to define a representative length  $\bar{L}_c$  of the average cycle which will be used as a model for the system. There are several strategies for this purpose. One approach is to remove any heavily abnormal cycle of the training set. These abnormalities usually appear when there are problems with the trigger signals  $p_p$  and  $p_v^\pm$ , especially with faulty R wave detection or PAC/PVC. The main effect of faulty triggers is that the faulty pulses will produce excessively large or short cycles that are easy to spot.

After cleaning the training set  $C_T$ , the representative length  $\bar{L}_c$  can be defined as the median of  $L_i^c$

$$\bar{L}_c = \text{median}\{L_i^c\}_{i=1}^{N_c}. \quad (1)$$

One advantage of the median over the average is that it is much less sensitive to a few large lengths  $L_i^c$ , that occur in faulty end cycle marks in  $p_p$  and  $p_v^\pm$ . The representative length  $\bar{L}_c$  can also identify outlier cycles in  $C_T$ .

With the new representative length  $\bar{L}_c$ , the sequences  $C_i$  are modified to have this length as follows; i) If  $L_i^c = \bar{L}_c$ , then  $C_i$  is not modified; ii) If  $L_i^c < \bar{L}_c$ , the length of  $C_i$  is augmented by adding the last image repeatedly to complete the length  $\bar{L}_c$ ; iii) If  $L_i^c > \bar{L}_c$ , the sequence  $C_i$  is truncated at  $\bar{L}_c$ . These modifications were shown to cause negligible discrepancies in the resulting averaged cycles. The discrepancies can be maintained small with proper choice of the training set (e.g., length of the training set and absence of disturbances as described before). No complications caused by these modifications were ever detected in our study.

By grouping the modified subsequences  $C_i$  in matrices  $C_i \in \mathbb{R}^{\ell \times \bar{L}_c}$  whose columns are the images of the cycle,  $C_i = [\mathbf{I}_1 \dots \mathbf{I}_{\bar{L}_c}]$ , the average cycle  $\bar{C}_T \in \mathbb{R}^{\ell \times \bar{L}_c}$  can be computed with the usual unbiased estimator

$$\bar{C}_T = [\bar{I}_1^c \dots \bar{I}_{\bar{L}_c}^c] = \frac{1}{N_c} \sum_{i=1}^{N_c} C_i, \quad (2)$$

where  $\bar{I}_k^c$  is the image of the average cycle at  $t_k$ . The columns of the average matrix  $\bar{C}_T$  represent, by hypothesis, images of the average cycle (ventilation or pulsatility).

One additional step is necessary in the case of the pulsatility cycle before taking the average (2). Due to the great amplitude of the ventilation cycle when compared to the amplitude of the pulsatility, it is necessary to remove the linear trend of the subsequences  $P_i$ . For that goal, a pixel-wise linear trend removal procedure must be done, that is, in each row of the matrices  $P_i$ .

In the case of the ventilation, the partial average ventilation cycles  $\bar{V}_T^\pm$  are joined to compose the average ventilation cycle  $\bar{V}_T \in \mathbb{R}^{\ell \times \bar{L}_v}$ , where  $\bar{L}_v = \bar{L}_v^+ + \bar{L}_v^-$

$$\bar{V}_T = [\bar{V}_T^+ \bar{V}_T^-]. \quad (3)$$

In principle, a single ventilation set of images  $V_i$ , comprising both inspiratory and expiratory phases could be created, slightly simplifying the training stage. However, computing these phases separately and joining only their averaged cycles results in an average cycle  $\bar{V}_T$  less prone to problems due to the variability of duration proportion between inspiratory/expiratory phases.

By the end of this step, average cycle matrices  $\bar{\mathbf{V}}_T \in \mathbb{R}^{\ell \times \bar{L}_v}$  and  $\bar{\mathbf{P}}_T \in \mathbb{R}^{\ell \times \bar{L}_p}$  will be determined.

**2.1.3. Dimensionality reduction with principal component analysis.** Under the perspective of dynamic systems, it is possible to conceive the average cycle  $\bar{\mathbf{C}}_T$  as a periodic system with  $\ell$  degrees of freedom (number of pixels). To reduce the dimensionality of the problem, that is, to eliminate those degrees of freedom that contribute little to the overall temporal dynamics of  $\bar{\mathbf{C}}_T$  and keep only the most relevant ones (herein denoted by *components*), principal component analysis (PCA) can be used [10]. The principal components are determined by performing the singular value decomposition (SVD) of the matrix  $\bar{\mathbf{C}}_T^\diamond \in \mathbb{R}^{\ell \times \bar{L}_c}$  where each row is given by the same row of  $\bar{\mathbf{C}}_T$  subtracted its mean

$$c_{ij}^\diamond = \bar{c}_{ij} - \frac{1}{\bar{L}_c} \sum_j \bar{c}_{ij}. \quad (4)$$

The SVD is given by

$$\bar{\mathbf{C}}_T^\diamond = \sum_{i=1}^r \mathbf{u}_i^c \sigma_i^c (\mathbf{v}_i^c)^\top, \quad (5)$$

where  $r = \min(\ell, \bar{L}_c)$ , the vectors  $\mathbf{u}_i^c \in \mathbb{R}^\ell$  and  $\mathbf{v}_i^c \in \mathbb{R}^{\bar{L}_c}$  are the left and right singular vectors and  $\sigma_1^c \geq \dots \geq \sigma_r^c \geq 0$  are the associated singular values [8]. The principal components are the vectors  $\mathbf{u}_i^c$  associated with the largest singular values  $\sigma_i^c$ . For this reason, we define the most important components those with associated singular values above a certain threshold that must be defined.

Let  $\mathcal{B}_c = \{\mathbf{u}_i^c\}_{i=1}^{N_u^c}$  be an ordered base for the subspace of images spanned by the principal components of  $\bar{\mathbf{C}}_T^\diamond$ , where  $N_u^c$  is the selected number of components. Then an image  $\mathbf{I}_k$  can be decomposed into

$$\mathbf{I}_k = \sum_{i=1}^{N_u^c} \alpha_i^c[k] \mathbf{u}_i^c + \mathbf{r}_k^c, \quad (6)$$

where  $\alpha_i^c[k] \in \mathbb{R}$  is the projection of  $\mathbf{I}_k$  into the direction of  $\mathbf{u}_i^c$ , and  $\mathbf{r}_k^c \in \mathcal{B}_c^\perp$  is the orthogonal residual. In matrix form

$$\mathbf{I}_k = \mathbf{U}_c \boldsymbol{\alpha}_k^c + \mathbf{r}_k^c \quad (7)$$

$$\mathbf{U}_c = [\mathbf{u}_1^c \ \dots \ \mathbf{u}_{N_u^c}^c] \quad (8)$$

$$\boldsymbol{\alpha}_k^c = [\alpha_1^c[k] \ \dots \ \alpha_{N_u^c}^c[k]]^\top, \quad (9)$$

where  $\mathbf{U}_c \in \mathbb{R}^{\ell \times N_u^c}$  is the *principal components matrix* whose columns are the vectors  $\mathbf{u}_i^c$ . The coordinate vector  $\boldsymbol{\alpha}_k^c \in \mathbb{R}^{N_u^c}$  is determined via the least squares solution of the quadratic error connected to (7)

$$e_k = \|\mathbf{I}_k - \mathbf{U}_c \boldsymbol{\alpha}_k^c\|_2^2, \quad (10)$$

given by

$$\boldsymbol{\alpha}_k^c = (\mathbf{U}_c^\top \mathbf{U}_c)^{-1} \mathbf{U}_c^\top \mathbf{I}_k = \mathbf{U}_c^\dagger \mathbf{I}_k, \quad (11)$$

where  $^\dagger$  represents the Moore-Penrose inverse [8]. It is worth stressing that recovering the projected image from  $\boldsymbol{\alpha}_k^c$  is straightforward

$$\mathbf{I}_k^c = \mathbf{U}_c \boldsymbol{\alpha}_k^c. \quad (12)$$

Provided that the choice of  $N_u^c$  makes  $\|r_k^c\|$  small enough, the images  $\mathbf{I}_k \in \mathbb{R}^\ell$  can be associated with the coordinate vector  $\boldsymbol{\alpha}_k^c$  of the space spanned by  $\mathcal{B}_c$ . Since in general  $N_u^c \ll \ell$ , this association drastically reduces the dimensionality of the problem, greatly facilitating the real-time image separation stage.

By the end of this step, bases  $\mathcal{B}_v = \{\mathbf{u}_i^v\}_1^{N_v^u}$  for ventilation and  $\mathcal{B}_p = \{\mathbf{u}_i^p\}_1^{N_p^u}$  for pulsatility cycles will be established with associated image projection equations of the form of (7)–(9)

$$\mathbf{I}_k = \mathbf{U}_v \boldsymbol{\alpha}_k^v + r_k^v \quad (13)$$

$$\mathbf{I}_k = \mathbf{U}_p \boldsymbol{\alpha}_k^p + r_k^p \quad (14)$$

**2.1.4. Evolution model of the average cycles.** To better understand the necessity of this step, it is worth having a sneak preview of the second stage, when images will be decomposed into ventilation and pulsatility. Briefly, each new image will be projected into the subspaces spanned by  $\mathcal{B}_{v,p}$  to minimize the 2-norm of the joint residual  $\mathbf{r}_k = \mathbf{I}_k - \mathbf{U}_v \boldsymbol{\alpha}_k^v - \mathbf{U}_p \boldsymbol{\alpha}_k^p$ . However, these bases are not mutually orthogonal in general, so this naive approach will fail to produce good separation in most cases. To overcome this problem we propose additional prior information terms in the residual minimization problem; the prior information will be based on evolution models of ventilation and pulsatility cycles. We propose using the average cycle  $\bar{\mathbf{C}}_T^\diamond$  to estimate an evolution model [9, 14].

First all images (columns) of  $\bar{\mathbf{C}}_T^\diamond$  are projected into  $\text{span}\{\mathcal{B}_c\}$  with (11)

$$\bar{\mathbf{C}}_T^\alpha = \mathbf{U}_c^\dagger \bar{\mathbf{C}}_T^\diamond, \quad (15)$$

where  $\bar{\mathbf{C}}_T^\alpha \in \mathbb{R}^{N_u^c \times \bar{L}_c}$  is the average cycle matrix in terms of the coordinate vector  $\bar{\boldsymbol{\alpha}}_k^c$  (columns). Each row of this matrix represents the discrete-time sequence of the projection coefficients  $\bar{\alpha}_i^c[k]$ .

Idealizing that the underlying system producing  $\bar{\mathbf{C}}_T^\alpha$  can be approximated by a linear and time-invariant model [7], the discrete-time transition matrix  $\Phi^c \in \mathbb{R}^{N_u^c \times N_u^c}$  can be defined such that [7]

$$\boldsymbol{\alpha}_{k+1}^c = \Phi^c \boldsymbol{\alpha}_k^c, \quad (16)$$

for all  $k = 1, \dots, \bar{L}_c$ . Finding a single matrix  $\Phi^c$  that can transition from  $\boldsymbol{\alpha}_k^c$  to  $\boldsymbol{\alpha}_{k+1}^c$  for all  $k$  is very unlikely, therefore a least square approach is employed. This approach can find reasonable approximations to  $\Phi^c$  as long as  $\bar{L}_c > N_u^c$ , which is usually the case.

Based on the definition (16), it is possible to pile sequences of coefficients column-wise so that

$$[\bar{\boldsymbol{\alpha}}_2^c \quad \bar{\boldsymbol{\alpha}}_3^c \quad \dots \quad \bar{\boldsymbol{\alpha}}_{\bar{L}_c}^c \quad \bar{\boldsymbol{\alpha}}_1^c] = \Phi^c [\bar{\boldsymbol{\alpha}}_1^c \quad \bar{\boldsymbol{\alpha}}_2^c \quad \dots \quad \bar{\boldsymbol{\alpha}}_{\bar{L}_c}^c]. \quad (17)$$

Note that periodicity is enforced with  $\bar{\boldsymbol{\alpha}}_1^c = \Phi^c \bar{\boldsymbol{\alpha}}_{\bar{L}_c}^c$ . This matrix equation can be solved for  $\Phi^c$  in the least square sense by

$$\Phi^c = [\bar{\boldsymbol{\alpha}}_2^c \quad \bar{\boldsymbol{\alpha}}_3^c \quad \dots \quad \bar{\boldsymbol{\alpha}}_{\bar{L}_c}^c \quad \bar{\boldsymbol{\alpha}}_1^c] [\bar{\boldsymbol{\alpha}}_1^c \quad \bar{\boldsymbol{\alpha}}_2^c \quad \dots \quad \bar{\boldsymbol{\alpha}}_{\bar{L}_c}^c]^\dagger. \quad (18)$$

The eigenvalues of the transition matrix represent the poles of the system, which are related to frequency, damping, and instability. The computed transition matrix is only an approximation and may introduce artificial damping or instabilities to the model. These issues can be resolved by manipulating the eigenvalues of  $\Phi^c$  without affecting the associated frequency [7].

Given the eigendecomposition of  $\Phi^c = \mathbf{W} \mathbf{Z} \mathbf{W}^{-1}$ , where  $\mathbf{W}$  is a matrix containing its eigenvectors and  $\mathbf{Z} \in \mathbb{R}^{N_u^c \times N_u^c}$  is a diagonal matrix containing the eigenvalues  $z_i \in \mathbb{C}$ , the following procedure is applied to each  $z_i$ :

1. Use the relation between the Laplace transform of a sampled signal and the  $Z$  transform  $z_i = \exp(s_i T_s)$  to find the associated continuous-time pole  $s_i$

$$s_i = \frac{\ln(z_i)}{T_s}, \quad (19)$$

where  $T_s$  is the sampling period.

2. Damping and instabilities are removed by moving the pole to the imaginary axis, keeping its magnitude

$$s'_i = \begin{cases} |s_i|j & \text{if } \operatorname{Im}(s_i) > 0, \\ -|s_i|j & \text{if } \operatorname{Im}(s_i) < 0 \end{cases} \quad (20)$$

where  $j$  is the imaginary unit.

3. The first step is reverted

$$z'_i = \exp(s'_i T_s), \quad (21)$$

Figure 2 presents a diagram of the three steps required to remove damping and instabilities of the poles.

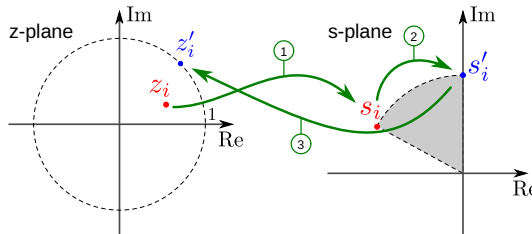


FIGURE 2. Eliminating damping and instabilities of the poles.

Finally, the modified transition matrix can be composed

$$\tilde{\Phi}^c = \mathbf{W} \mathbf{Z}' \mathbf{W}^{-1}, \quad (22)$$

where  $\mathbf{Z}'$  is a diagonal matrix of the modified eigenvalues  $z'_i$ . For brevity of notation, the  $\tilde{\cdot}$  mark of the modified transition matrix will be dropped. As a final observation, when the chosen number of principal components is  $N_u^c = 1$ , the resulting transition matrix is the trivial matrix  $\Phi^c = [1]$ .

By the end of this step, modified transition matrices  $\Phi^{v,p}$  will be defined.

**2.1.5. Offset component.** Before proceeding with the second stage, one extra component must be included to accommodate the offset (uniform) level of the images. The component is uniform  $\mathbf{u}_1^u = \frac{1}{\sqrt{\ell}} \mathbf{1}$ , where  $\mathbf{1} \in \mathbb{R}^\ell$  is a vector whose components are all equal to one. The principal components matrix is  $\mathbf{U}_u = [\mathbf{u}_1^u] \in \mathbb{R}^{\ell \times 1}$  and its transition matrix is  $\Phi^u = [1]$ .

The rationale for this inclusion lies in the fact that both ventilation and pulsatility models are obtained from zero-mean sequences (5), however, there is no reason to believe that the images are zero mean over time due to progressive changes in the patient. The attempt to split the signal into ventilation and pulsatility only would result in  $\mathbf{I}_k = \mathbf{U}_v \boldsymbol{\alpha}_k^v + \mathbf{U}_p \boldsymbol{\alpha}_k^p + \mathbf{r}_k$ , and offset components would be mixed with the

remaining less predictable residual components. Therefore it makes sense to split the residual into the offset component and the other part  $\mathbf{I}_k = \mathbf{U}_v \boldsymbol{\alpha}_k^v + \mathbf{U}_p \boldsymbol{\alpha}_k^p + \mathbf{U}_u \boldsymbol{\alpha}_k^u + \mathbf{r}_k$ .

**2.2. Real-time image separation stage.** We propose a cost function minimization method to separate mixed images  $\mathbf{I}_k$  (not present in the training set) into ventilation  $\mathbf{I}_k^v \in \text{span}\{\mathcal{B}_v\}$ , blood pulsatility  $\mathbf{I}_k^p \in \text{span}\{\mathcal{B}_p\}$ , and offset  $\mathbf{I}_k^u \in \text{span}\{\mathcal{B}_u\}$  components. The process is performed in terms of their low-dimensional coordinate vectors  $\boldsymbol{\alpha}_k^{v,p,u}$ .

The spaces spanned by  $\mathcal{B}_{v,p,u}$  are not guaranteed to be mutually orthogonal. The probability of them being mutually orthogonal is very small because ventilation and pulsatility processes share a large area of influence in the chest. Therefore, a naive approach to minimizing the norm of the joint residual  $\mathbf{r}_k = \mathbf{I}_k - \mathbf{U}_v \boldsymbol{\alpha}_k^v - \mathbf{U}_p \boldsymbol{\alpha}_k^p - \mathbf{U}_u \boldsymbol{\alpha}_k^u$  would not be effective. We propose using the evolution models of the form of (16), already estimated in the training stage as dynamic prior information for the separation [11].

We propose the following regularized least mean-square (LMS) problem

$$\begin{aligned} \underset{\boldsymbol{\alpha}_k^v, \boldsymbol{\alpha}_k^p, \boldsymbol{\alpha}_k^u}{\text{minimize}} \quad & \left\{ \|\mathbf{I}_k - \mathbf{U}_v \boldsymbol{\alpha}_k^v - \mathbf{U}_p \boldsymbol{\alpha}_k^p - \mathbf{U}_u \boldsymbol{\alpha}_k^u\|_2^2 + \beta_v^2 \|\Phi^v \boldsymbol{\alpha}_{k-1}^v - \boldsymbol{\alpha}_k^v\|_2^2 \right. \\ & \left. + \beta_p^2 \|\Phi^p \boldsymbol{\alpha}_{k-1}^p - \boldsymbol{\alpha}_k^p\|_2^2 + \beta_u^2 \|\Phi^u \boldsymbol{\alpha}_{k-1}^u - \boldsymbol{\alpha}_k^u\|_2^2 \right\}, \end{aligned} \quad (23)$$

where the second, third, and fourth terms penalize solutions that deviate from the predictions of the evolution models. The vectors  $\boldsymbol{\alpha}_{k-1}^{v,p,u}$  are the separation solution of the previous discrete time  $t_{k-1}$ . The scalars  $\beta_{v,p,u} > 0$  serve as regularization parameters for the minimization problem.

The problem can be concatenated as

$$\begin{aligned} \underset{\boldsymbol{\alpha}_k^v, \boldsymbol{\alpha}_k^p, \boldsymbol{\alpha}_k^u}{\text{minimize}} \quad & \left\{ \|\mathbf{I}_k - \mathbf{U} \boldsymbol{\alpha}_k\|_2^2 + \|\Phi \boldsymbol{\alpha}_{k-1} - \mathbf{B} \boldsymbol{\alpha}_k\|_2^2 \right\} \\ \boldsymbol{\alpha}_k &= [\boldsymbol{\alpha}_k^v \quad \boldsymbol{\alpha}_k^p \quad \boldsymbol{\alpha}_k^u]^\top \\ \mathbf{U} &= [\mathbf{U}_v \quad \mathbf{U}_p \quad \mathbf{U}_u] \\ \Phi &= \text{blkdiag}(\beta_v \Phi^v, \beta_p \Phi^p, \beta_u \Phi^u) \\ \mathbf{B} &= \text{blkdiag}(\beta_v \mathbb{I}_{N_v^v}, \beta_p \mathbb{I}_{N_u^p}, \beta_u \mathbb{I}_1) \end{aligned} \quad (24)$$

where  $\mathbb{I}_n$  is the  $n \times n$  identity matrix and the solution in stacked form is given by

$$\hat{\boldsymbol{\alpha}}_k = [\mathbf{U}]^\dagger \begin{bmatrix} \mathbf{I}_k \\ \Phi \boldsymbol{\alpha}_{k-1} \end{bmatrix}. \quad (25)$$

The real-time separation stage requires only evaluating (25) once per input image  $\mathbf{I}_k$  and the resulting ventilation and pulsatility images can be generated using (12). Note that the pseudoinverse operation depends exclusively on  $\mathbf{U}$  and  $\mathbf{B}$  and, as long as the main components and  $\beta_{v,p,u}$  do not change, can be computed at the end of the training stage and stored in memory to reduce the computational load in this stage.

**2.2.1. Evolution model update.** The evolution model might need updates regularly to accommodate physiological changes. One of the most common changes that can happen very often is changes in ventilation or cardiac rates. If the changes are restricted to frequency only, that is, there are no substantial changes in  $\mathbf{U}_c$  and the changes in  $\bar{\mathbf{C}}_T^\alpha$  are only due to time scaling, then there is a fast way to update the evolution model.

Let  $f^c = \frac{1}{L_c} f_s$  be the current frequency of the average cycle  $\bar{\mathbf{C}}_T^\alpha$  and  $f_{\text{new}}^c$  be the new frequency, obtained by any available method (e.g., measured with additional equipment connected to the patient, or functional image analysis). The discrete-time transition matrix  $\Phi^c$  can be updated by changing all its eigenvalues  $z_i$ . The frequency associated with a pole is given by its argument; therefore, the modified pole  $z'_i$  due to a change from  $f^c$  to  $f_{\text{new}}^c$  is a new complex number with a proportionally modified argument while keeping the magnitude unaltered. The damping and instability elimination procedure in the training stage made the poles unit length, therefore the updated poles are given by

$$z'_i = \exp \left( j \frac{f_{\text{new}}^c}{f^c} \theta_i \right), \quad (26)$$

for all  $i = 1, \dots, N_u^c$ , where  $\theta_i$  is the argument of the original pole  $z_i$ . This procedure is suitable for real-time applications because the eigendecomposition of the transition matrix can be stored in the training stage, the operation (22) can be quickly computed, and the resulting updated transition matrix does not appear in the pseudoinverse of (25).

**3. Experimental data collection and EIT image generation.** The experimental protocol was performed at the Research and Education Institute of Sírio-Libanês Hospital (São Paulo, Brazil) and was approved by the Institutional Animal Research Ethics Committee (CEUA 2011/14). It was performed according to the National Institutes of Health guidelines for the use of experimental animals.

The animals were sedated with propofol and remifentanil titrated to effect. Subject 1 was maintained under pressure-controlled ventilation mode during the whole experiment. Subject 2 went through various ventilation mode changes, including changes in ventilation frequency, ventilation pauses, and PEEP and tidal volume changes.

Difference EIT images were generated using Timpel's Enlight 1800 at a rate of 50 images per second ( $f_s = 50$  Hz). The device has 32 electrodes injecting 1.0 mA pairwise *skip-3* current pattern [12] at 125 kHz and measuring differential voltages also following a *skip-3* pattern. The reference frame of the difference images is the average over a few ventilatory cycles.

The difference images were generated from the linearized observation model in terms of resistivity [15], with added Gaussian smoothness and uniform sensitivity priors. The resulting images are  $32 \times 32$  pixels, with a total of 745 valid pixels, that is, pixels that represent the thorax of the subject. In our analysis, the images are vectors in  $\mathbb{R}^{745}$ . The images are normalized with respect to the average resistivity of the chest and, therefore, are non-dimensional. All EIT images presented in the next sections are non-dimensional.

#### 4. Results.

**4.1. Training stage.** A sequence of 4901 images was used as training dataset  $\mathcal{S}_T = \{\mathbf{I}_k\}_1^{4901}$ . The dataset was split into  $N_p = 284$  pulsatility,  $N_v^+ = 26$  inspiration, and  $N_v^- = 25$  expiration cycles and the average cycles  $\bar{\mathbf{P}}_T$  and  $\bar{\mathbf{V}}_T$  were determined from them (equation (2)). Figure 3 presents the images of the average pulsatility  $\bar{\mathbf{P}}_T^\diamond$  and ventilation  $\bar{\mathbf{V}}_T^\diamond$  cycles of the first swine subject. The heart and lung regions are highlighted for better visualization and the arrow indicates time direction. The average cycles are composed of  $\bar{L}_p = 18$  and  $\bar{L}_v = 188$  images.

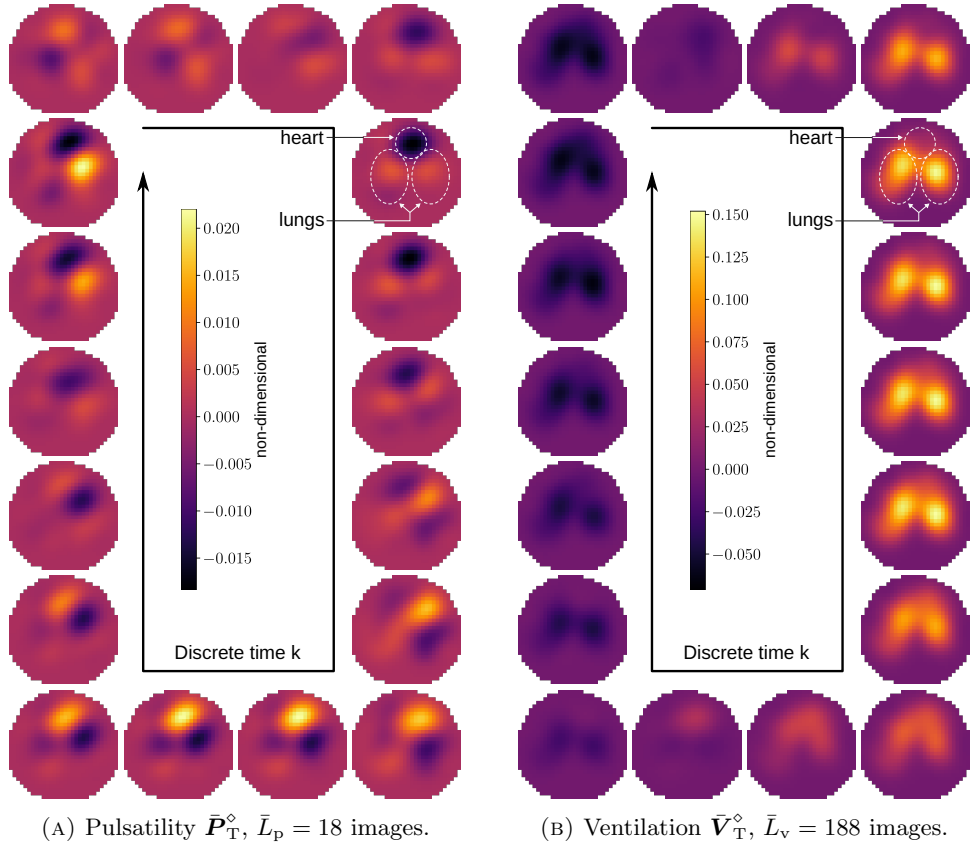


FIGURE 3. Representative sequence of images of the average pulsatility  $\bar{P}_T^\diamond$  (left) and ventilation  $\bar{V}_T^\diamond$  (right) obtained from EIT images of the first swine subject. Time increases in the clockwise direction. Not all images of the ventilation cycle are presented in this figure.

The first eight principal components of pulsatility  $\mathbf{u}_i^p$  (left) and ventilation  $\mathbf{u}_i^v$  (right) are presented in Figure 4, as well as the associated singular values (equation (5)). The singular values are normalized with respect to the largest singular value  $\tilde{\sigma}_i^c = \sigma_i^c / \sigma_1^c$ . Note that the singular values of the pulsatility cycle decrease more slowly than in the ventilation cycle. For example,  $\tilde{\sigma}_4^p$  is about 11.5% of the largest singular value whilst  $\tilde{\sigma}_4^v$  is only 1.6%. Consequently, in general, more principal components are necessary for the pulsatility cycle modeling.

Figure 5 shows the changes of the first four components of the reduced dimensional average cycles  $\bar{P}_T^\alpha$  (left) and  $\bar{V}_T^\alpha$  (right) (equation (15)) over the cycle. Note that the first components have the largest variations along the cycles. The first component of pulsatility  $\mathbf{u}_1^p$  depicts blood flowing from the top central region (heart) to the sides (lungs). The next components depict asymmetries of the pulsatility between the lungs and inside each lung. However, these asymmetries are much smaller than the first (main) component for this subject. The coefficients of the ventilation cycle display some oscillations, especially during the end of the expiration (end of the cycle). The oscillation comes from the residual pulsatility signal in

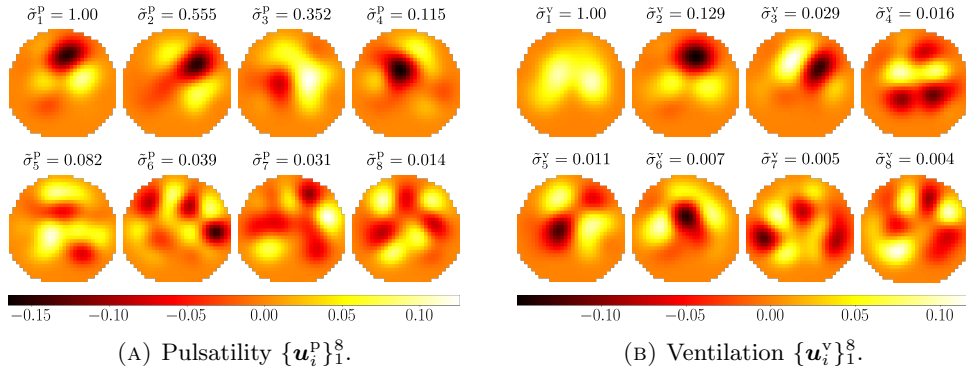


FIGURE 4. First eight principal components of pulsatility  $\bar{\mathbf{P}}_T^\diamond$  (left) and ventilation  $\bar{\mathbf{V}}_T^\diamond$  (right) of the first swine subject. Each component is accompanied by the associated normalized singular value.

the average cycle. The increase of pulsatility at the end of expiration might be due to the reduced air pressure in the airways, allowing the blood vessels in the lungs to expand more in response to the blood pressure waves and, therefore, increase the pulsatility in the images.

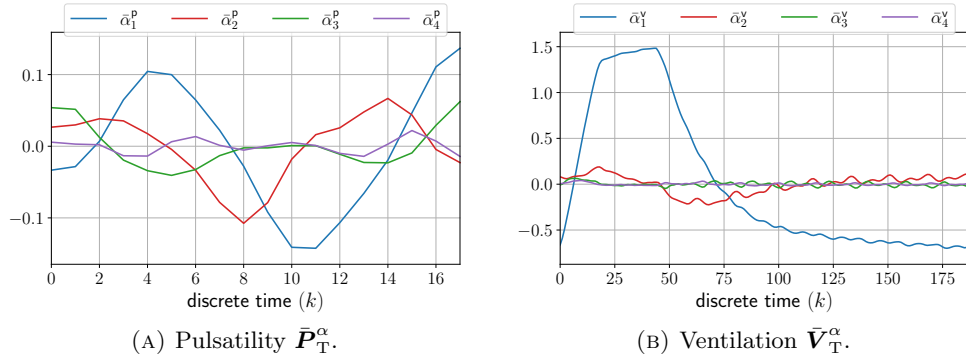


FIGURE 5. Discrete time sequence of the four principal components of the average pulsatility and ventilation cycles over one cycle of the first swine subject.

Next, ventilation and pulsatility transition matrices were computed (equation (18)) with  $N_u^P = N_u^V = 8$  principal components, followed by eigenvalue modification (22) to remove damping. Figure 6 presents comparisons of the coefficients  $\bar{\alpha}_k^{v,p} \in \mathbb{R}^8$  (dashed black lines) and the predicted values  $\hat{\alpha}_k^{v,p} = \Phi^{v,p} \bar{\alpha}_{k-1}^{v,p}$  of the pulsatility (top) and ventilation (bottom). The gray subplots display the relative error of the prediction, defined as  $e_r^{v,p} = \frac{|\bar{\alpha}_k^{v,p} - \hat{\alpha}_k^{v,p}|}{\max_k \{\bar{\alpha}_k^{v,p}\}}$ , where the operations are element-wise. Note that the two first components of the pulsatility (dashed line) have a considerably large jump between the last and the first frames. This jump is reduced in the model prediction (red line) due to the periodicity imposition  $\bar{\alpha}_1^P = \Phi^P \bar{\alpha}_{L_p}^P$  during the construction of the transition matrix.

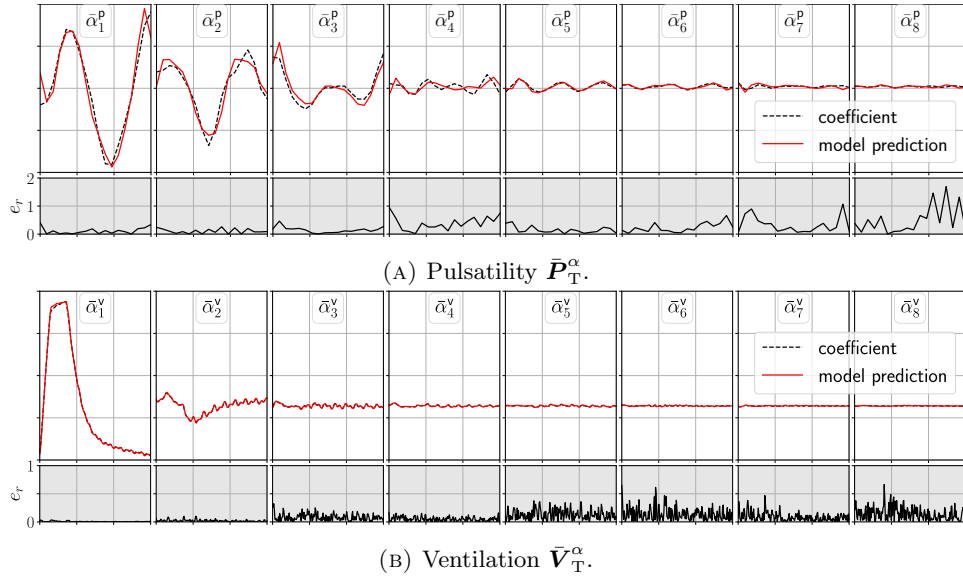


FIGURE 6. Comparison between the coefficients  $\bar{\alpha}_k^{v,p}$  (dashed black lines) and the predicted values  $\hat{\alpha}_k^{v,p}$  (red) of the first subject. The gray plots display the relative error of the predictions.

Although the errors increase with the index of the coefficients, their importance to the total description of the average cycles decreases fast as their singular values drop to zero quickly (see Figure 4).

**4.2. Real-time image separation stage.** A new sequence of 6700 EIT images ( $\approx 136$  s) of the first subject was used as input for the real-time separation stage. The set of hyperparameters is: singular value threshold of 10% (resulting in  $N_u^v = 2$  and  $N_u^p = 4$ ),  $\beta_v = \beta_p = 0.01$ , and  $\beta_u = 1.0$ . No retraining stage was used.

Figure 7 presents plots of the sum of the pixels of the images  $I_k$  in the sequence and their decomposition

$$\overbrace{I_k}^{\text{input}} = \underbrace{\mathbf{U}_v \bar{\alpha}_k^v}_{\text{ventilation}} + \underbrace{\mathbf{U}_p \bar{\alpha}_k^p}_{\text{pulsatility}} + \underbrace{\mathbf{U}_p \bar{\alpha}_k^u}_{\text{offset}} + \overbrace{r_k}^{\text{residual}}. \quad (27)$$

The sum of the pixels is an approximation to the plethysmograph of the subject, depicting the overall dynamics of the chest.

The plethysmograph of the input depicts a large variation between -15 to +22 relative to ventilation and a much faster and smaller oscillation associated with blood pulsatility. These effects can be better distinguished in the right column which presents a zoomed plot of the highlighted region. The total LMS plethysmograph is very similar to the input and the residual is very small ( $\approx 10^{-1}$ ) showing that the decomposition (27) was successful in assigning most of the signal into either ventilation, pulsatility, and offset.

The ventilation plethysmograph is smoother than the plethysmograph of the input signal and most of the pulsatility signal is present in the correct component. There is still a small portion of pulsatility signal in the ventilation component and

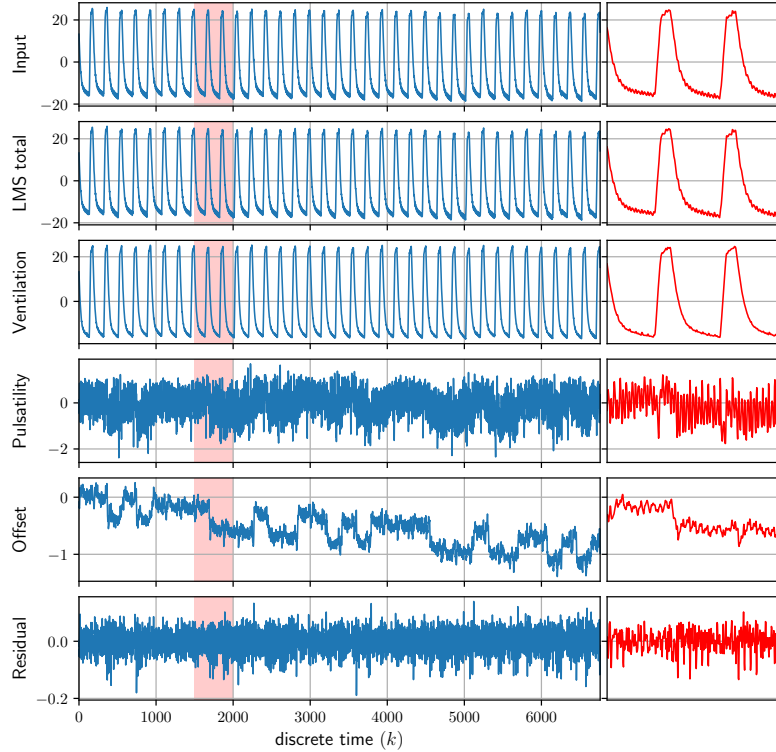


FIGURE 7. Time history of the sum of the pixels of the images of the first subject. From top to bottom: Input, LMS total, Ventilation, Pulsatility, Offset, and Residual components, as defined in (27). The right column of plots presents zoomed plots of the highlighted regions on the left.

vice-versa. Figure 8 displays the EIT input, ventilation, and pulsatility images along one ventilation cycle.

EIT images of a second subject were used to test the proposed method. A sequence of 4901 images was collected for training. The training dataset contained  $N_p = 171$  pulsatility,  $N_v^+ = 49$  inspiration, and  $N_v^- = 48$  expiration cycles. For this subject, the set of hyperparameters is: singular value threshold of 5% (resulting in  $N_u^v = 2$  and  $N_u^p = 4$ ),  $\beta_v = \beta_p = 0.01$ , and  $\beta_u = 1.0$ . Figure 9 displays the four principal components of pulsatility and ventilation of the second subject.

For the real-time image separation, a sequence of 25000 images ( $\approx 500$ s) was collected. Ventilation mode was modified several times during data collection. Variations included significant changes in ventilation frequency, tidal volume, ventilation pauses, and PEEP changes. No changes in the pulsatility cycle were intentionally induced. These variations can be seen in Figure 10 that displays the sum of the pixels of each image. The leftmost column presents the plethysmographs of the entire dataset and the other columns present zoomed plots of the color-coded highlighted regions. It is important to stress that a single training stage was performed and was used for the entirety of the 25000 images. The goal is to test its robustness to variations.

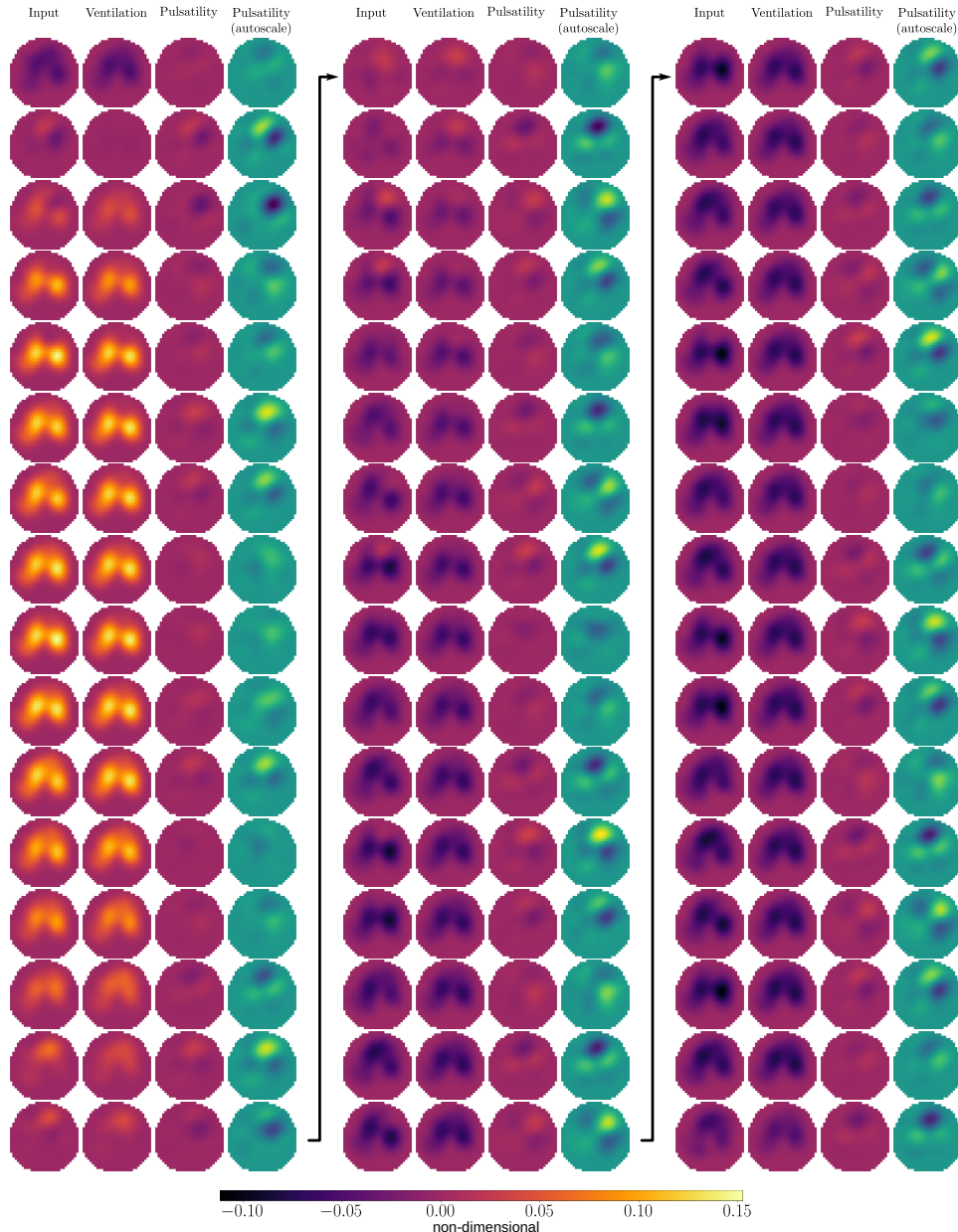


FIGURE 8. Time sequence of ventilation and pulsatility separation along one ventilation cycle of the first subject. From left to right: input images  $\mathbf{I}_k$ , ventilation component  $\mathbf{I}_k^v$ , and pulsatility component  $\mathbf{I}_k^p$  using two color maps, the first with the same color map and limits of the other images and the second using another colormap and auto-scale to increase contrast.

The red region in Figure 10 is similar to the dynamics of the training set, that is, the training set was collected using the same ventilation characteristics, therefore

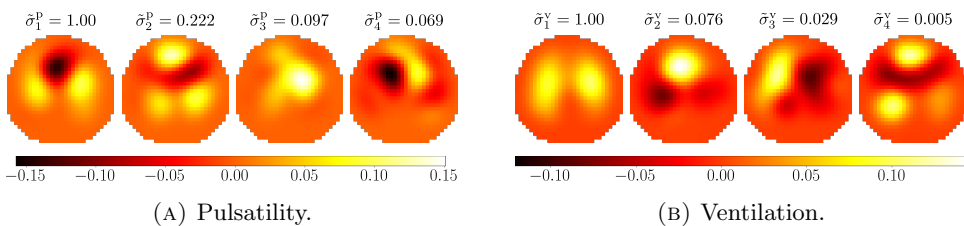


FIGURE 9. First four principal components of pulsatility  $\bar{P}_T^\diamond$  (left) and ventilation  $\bar{V}_T^\diamond$  (right) of the second swine subject. Each component is accompanied by the associated normalized singular value.

this region should be the most similar to the training set. Indeed, the red ventilation plethysmograph shows that only a small portion of the pulsatility is present. The green region is marked by halving the ventilation frequency. Again, ventilation and pulsatility were successfully separated and just a small portion is still mixed. Note that the amplitude of the green pulsatility curve is slightly smaller than the red one, indicating that a portion of the pulsatility is in the ventilation component. The blue region is a ventilation pause when the ventilator is paused at the end of the expiration. In this region, no ventilation signal is present. Here we can see that no ventilation appears in the blue plots. The trained ventilation model is far from being adequate for the blue region, nevertheless, the method still adequately separates the images. Note that the amplitude of the pulsatility signal varies significantly with the ventilatory phase (red and green), in contrast with the stable amplitude during the breath hold (blue). The magenta region is marked by considerable changes in PEEP and tidal volume. Again, the method was capable of separating the images.

To evaluate the separation in the heart and lungs regions in the second subject in more detail, three small regions of interest (ROIs) were segmented by a specialist that belong to the heart, to the left, and to the right lungs. They are presented in Figure 11. Each ROI is composed of six pixels.

The plethysmographs of these three ROIS can be seen in Figure 12. The separation in each ROI (rows) is presented for each of the four colored windows in Figure 10 (columns). From top to bottom, the results from the heart, and the left and right lungs ROIs are presented. The black lines are the input image plethysmographs of each ROI, while the colored plots present ventilation and pulsatility signals. The pulsatility plot was presented separately in the grayed region for clarity. It is evident that the separation was successful, very small ventilatory signal is present in the pulsatility and vice-versa. Note that the heart region still possesses a significant ventilation signal. This might be an EIT artifact, caused by the Gaussian smoothness prior or an evidence of heart-lung interactions caused by variations in pleural and transpulmonary pressures during the ventilatory cycle [13]. There is no reason to believe that this could be caused by the proposed method since this mixture is already presented in the input plethysmograph (black line).

**5. Discussion.** The analysis of live subject signals is generally very challenging due to differences between individuals, physiological changes, sudden events, movement interference, faulty measurements, and other sources of disruption, such as additional equipment connected to the subject. What works well for one subject may not work well for another, or even for the same subject at a later time. Devices

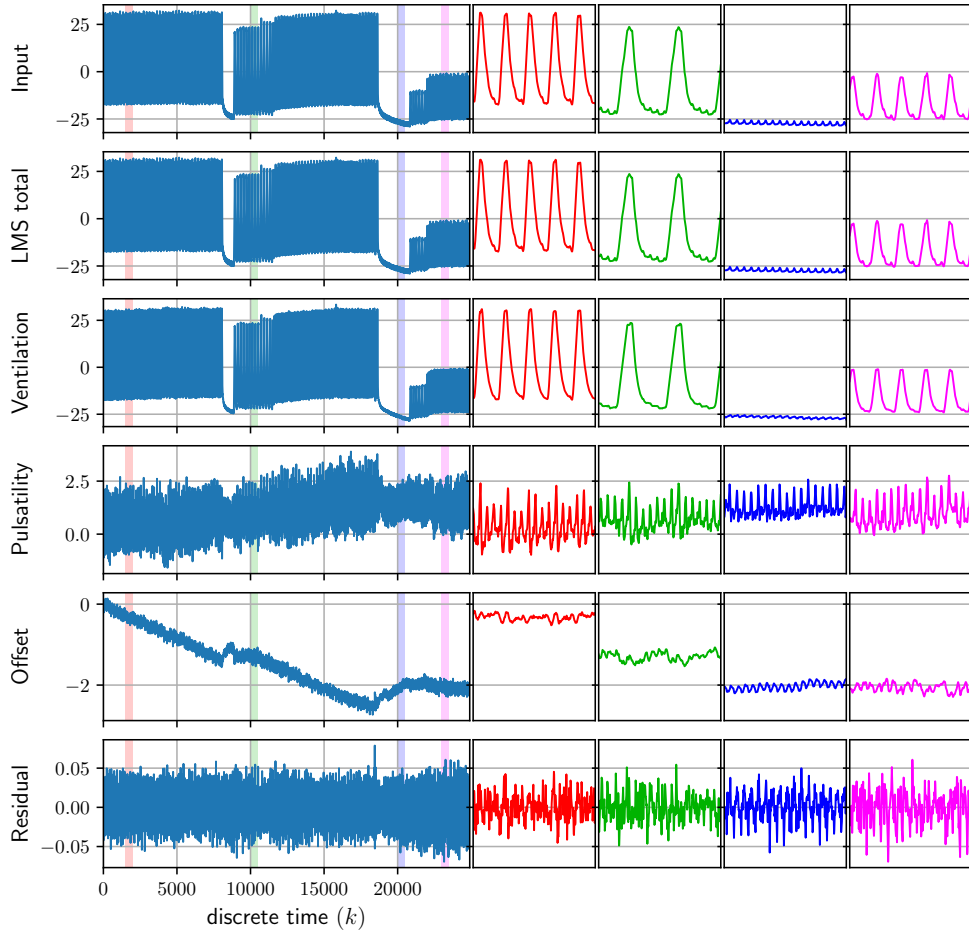


FIGURE 10. Time history of the sum of the pixels of the images of the second subject. From top to bottom, input, LMS total, ventilation, pulsatility, offset, and residual components as defined in (27). The left column displays the entire dataset and the next columns present zoomed plots of the colored highlighted regions on the left column. The red region is similar to the dynamics present in the training set, the green region has ventilatory frequency halved, the blue region has a ventilation pause, and the magenta has changes to the tidal volume and PEEP.

responsible for acquiring and processing these signals must deal with this problem. It is desirable to personalize the device settings, but it might not be possible to reach optimal settings on hospital premises due to time and equipment constraints. This problem is even greater with real-time monitoring equipment that has limited time to adjust and optimize its settings.

In practice, it is common to take a conservative approach to adjusting the algorithms used in these devices to increase robustness. The idea is to accept a compromise solution that balances optimal settings with robustness against variations. For an algorithm that involves minimizing a cost function in the form of



FIGURE 11. Region of interest of the heart (red), left, and right lungs (yellow) of the second subject, segmented by a specialist. Each area is composed of 6 pixels.

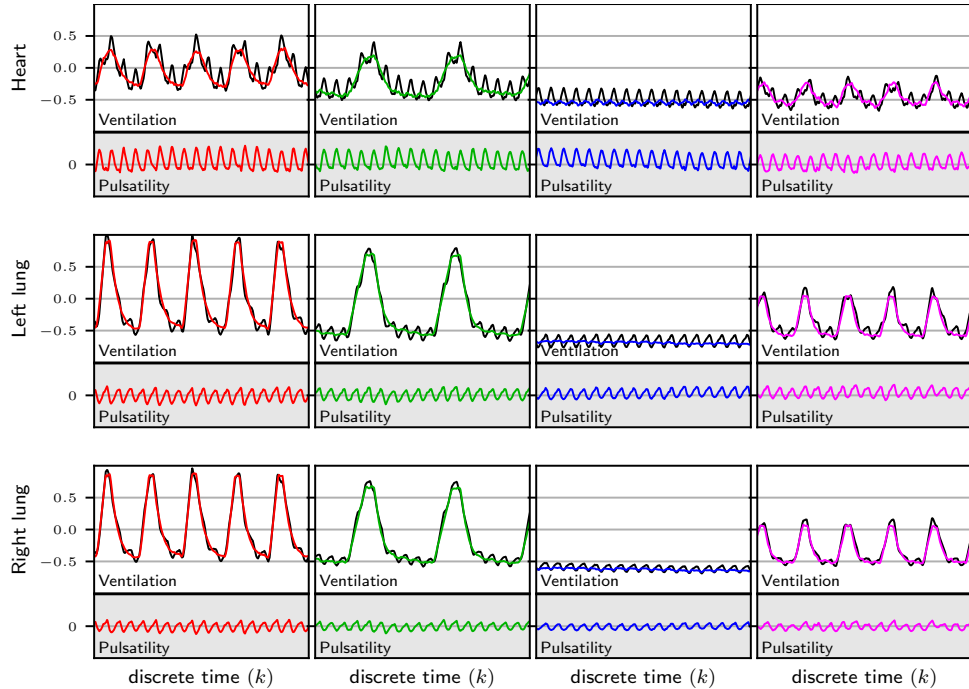


FIGURE 12. Time history of the sum of the pixels of the ROIs of the heart (top row), left lung (middle row), and right lung (bottom row.) in each of the colored highlighted segments of Figure 10 of the second subject. The black lines are the sum of the pixels of the input images in each ROI, while the colored plots are the separated ventilation and pulsatility. The pulsatility plot was presented separately in the grayed region for clarity.

(24), the compromise solution requires accepting suboptimal hyperparameters that still guarantee good solutions and robustness. In our case, the hyperparameters are (i) the length of the training set  $\mathcal{S}_T$ , (ii) the periodicity at which the training stage

is executed to update the average cycles and their evolution models, (iii) the regularization parameters  $\beta_{v,p,u}$ , and (iv) the principal components selection to form the bases  $\mathcal{B}_{v,p}$ .

In our tests with EIT experimental data, collecting 4900 images ( $\approx 130$  s) for the training set was enough. This number of images allowed the collection of a sufficiently large number of cycles for the averages. Care was taken to ensure that the ventilation mode was the same in the time interval for the training set. This amount of time is reasonable in clinical applications for this type of monitoring. The analysis of subject 2 shows that the separation was successful making it possible to capture the changes in pulsatility that occurred due to heart-lung interactions (Figure 10), even with significant changes in the ventilation characteristics in the real-time separation stage. This indicates that the method is robust to moderate changes and suggests its potential to pave the way for new advancements in the study of functional hemodynamics with EIT. In the case of substantial changes, it might be beneficial to train again. The regularization parameters were chosen using a simple search method in the range  $[10^{-3}, 10^2]$ , characterizing a suboptimal search method that could be improved. The search for the best values observed the separation of the images and the overall robustness against variations previously mentioned. Curiously, the same set of regularization parameters was effective for both subjects. This, however, does not imply that the same parameters would work in other cases.

The choice of the principal components is the hyperparameter with the highest influence over the performance of the proposed method and requires special attention. The general rule is to select the components associated with the largest singular values. The rationale behind this choice lies in the fact that these components represent the majority of the variations observed in the data. In the case of a dynamic system, the time behavior of the average cycles. In general, the more components the better the approximation is. However, since  $\mathcal{B}_{v,p}$  are not mutually orthogonal, the first term of (24) might ‘leak’ part of the ventilation component to the pulsatility component and vice-versa. The smaller the singular value, the more oscillatory the associated singular vector (see Figure 4) and the higher the chances that ventilation and pulsatility components become similar. Therefore it is beneficial to truncate the models. In this work, the selection of the principal components is based on a threshold value applied to the normalized singular values. In our studies, threshold values between 2% and 15% produced good separations.

**5.1. Timing considerations.** The method was implemented in C and executed in an 8x11th Gen Intel® Core™ i5-11300H 3.10 GHz laptop running Kubuntu 22.04.4 LTS. The real-time image separation stage took 60.30 s to separate 32000 images, including evolution model update (see Section 2.2.1), resulting in 1.87 ms per image in average. The time required to separate the image is much smaller compared to the time necessary to generate it in our EIT device ( $\approx 0.02$  s), characterizing a real-time method in practical terms.

**5.2. Limitations and further developments.** The proposed method has limitations. The bases  $\mathcal{B}_{v,p}$  are not mutually orthogonal and part of the pulsatility might be present in the ventilation signal and vice-versa. The regularization terms in (23) aim to minimize this problem. One possibility to further reduce the residual mixture is to employ digital filters as a post-processing step. However, this procedure would add delays to the separation. Another limitation is the linear model

used as prior information. The model has limitations to describe complex processes. Fortunately, the method allows replacing the model with another with relative ease although it could require more computation time in the image separation stage.

Model uncertainties can be compensated by adjusting the regularization parameters  $\beta_{v,p,u}$  in the real-time separation stage. However, we need to consider that the model's time-invariance may cause issues during monitoring, as ventilation and pulsatility change over time. A fast and efficient method for updating the model in real-time when frequency changes are detected is presented in this paper. In case of more complex changes, the models might need updates with some periodicity. We did not explore methods to identify if/when the models need update in this paper.

In our experience with experimental data, the components associated with the largest singular values might not be the only selection criterion. When the correlation between the average cycles is high, usually happening when the period of the ventilation cycle is close to a multiple of the period of the pulsatility cycle, the average cycles  $\bar{P}_T$  and  $\bar{V}_T$  display a small portion of the other cycle. In this case, it might be a good strategy to discard such components. This possibility was not explored in this work. Another option is to avoid choosing components  $u^{v,p}$  that are too similar. This could be done by setting a direction cosine threshold between them.

The proposed method cannot separate ventilation and pulsatility if information about the latter is lost in the input images. We showed examples using EIT images, where pulsatility signals are usually ten times smaller than ventilation. The success of the separation strongly depends on the capacity of the EIT device to collect data where the blood pulsatility signal-to-noise ratio is such that this information is not lost to noise. In our experience, Timpel's Enlight 1800 EIT device is sensitive enough to generate images of the chest where pulsatility information is present. The sensitivity of other devices must be addressed.

**6. Conclusion.** We propose a functional image separation method to split tomographic images of the chest into ventilation and pulsatility. The method was evaluated with EIT images but this method is general and can be applied to other types of functional images. The main novelty of this method is finding an evolution model of the average cycles. The model is employed to incorporate a priori information during the real-time separation stage. The linear model matrix is calculated during the training stage and updated efficiently in real-time to accommodate changes in cardiac and respiratory frequencies. We demonstrated the effectiveness and robustness of the separation using experimental data.

## REFERENCES

- [1] J. B. Borges, F. Suarez-Sipmann, S. H. Bohm, G. Tusman, A. Melo, E. Maripuu, M. Sandström, M. Park, E. L. V. Costa, G. Hedenstierna and M. Amato, [Regional lung perfusion estimated by electrical impedance tomography in a piglet model of lung collapse](#), *Journal of Applied Physiology*, **112** (2012), 225-236.
- [2] D. Conen, M. Adam, F. Roche, J.-C. Barthelemy, D. Felber Dietrich, M. Imboden, N. Künzli, A. von Eckardstein, S. Regenass, T. Hornemann, T. Rochat, J.-M. Gaspoz, N. Probst-Hensch and D. Carballo, [Premature atrial contractions in the general population: Frequency and risk factors](#), *Circulation*, **126** (2012), 2302-2308.
- [3] E. L. Costa, R. G. Lima and M. B. P. Amato, [Electrical impedance tomography](#), *Current Opinion in Critical Care*, **15** (2009), 18-24.
- [4] J. M. Deibebe, H. Luepschen and S. Leonhardt, [Dynamic separation of pulmonary and cardiac changes in electrical impedance tomography](#), *Physiological Measurement*, **29** (2008), S1-S14.

- [5] A. Fagerberg, O. Stenqvist and A. Åneman, **Monitoring pulmonary perfusion by electrical impedance tomography: An evaluation in a pig model**, *Acta Anaesthesiologica Scandinavica*, **53** (2009), 152-158.
- [6] I. Frerichs, S. Pulletz, G. Elke, F. Reifferscheid, D. Schädler, J. Scholz and N. Weiler, **Assessment of changes in distribution of lung perfusion by electrical impedance tomography**, *Respiration*, **77** (2009), 282-291.
- [7] B. Friedland, *Control System Design: And Introduction to State-Space Methods*, 1st edition, Dover, New York, 2005.
- [8] G. H. Golub and C. F. Van Loan, *Matrix Computations*, 3rd edition, The Johns Hopkins University Press, 1996.
- [9] S. R. Ibrahim and E. C. Mikulcik, A method for the direct identification of vibrations parameters from the free response, *Shock and Vibration Bulletin*, **47** (1977), 183-198.
- [10] I. T. Jolliffe, *Principal Component Analysis*, 2nd edition, Springer Series in Statistics, Springer, New York, NY, 2002.
- [11] J. Kaipio and E. Somersalo, *Statistical and Computational Inverse Problems*, 1st edition, Springer, New York, 2005.
- [12] O. Luppi Silva, R. Gonzalez Lima, T. Castro Martins, F. Silva de Moura, R. Seiji Tavares and M. Sales Guerra Tsuzuki, **Influence of current injection pattern and electric potential measurement strategies in electrical impedance tomography**, *Control Engineering Practice*, **58** (2017), 276-286.
- [13] S. Magder, **Heart-lung interaction in spontaneous breathing subjects: The basics**, *Annals of Translational Medicine*, **6** (2018), 348-348.
- [14] F. S. Moura, J. C. C. Aya, A. T. Fleury, M. B. P. Amato and R. G. Lima, **Dynamic imaging in electrical impedance tomography of the human chest with online transition matrix identification**, *IEEE Transactions on Biomedical Engineering*, **57** (2010), 422-431.
- [15] P. J. Vauhkonen, M. Vauhkonen, T. Savolainen and J. P. Kaipio, **Three-dimensional electrical impedance tomography based on the complete electrode model**, *IEEE Transaction on Biomedical Engineering*, **46** (1999), 1150-1160.
- [16] M. von Rotz, S. Aeschbacher, M. Bossard, T. Schoen, S. Blum, S. Schneider, J. Estis, J. Todd, M. Risch, L. Risch and D. Conen, **Risk factors for premature ventricular contractions in young and healthy adults**, *Heart*, **103** (2016), 702-707.
- [17] A. Vonk-Noordegraaf, A. Janse, J. T. Marcus, J. G. F. Bronzwaer, P. E. Postmus, T. J. C. Faes and P. M. J. M. de Vries, **Determination of stroke volume by means of electrical impedance tomography**, *Physiological Measurement*, **21** (2000), 285. <http://stacks.iop.org/0967-3334/21/i=2/a=308>.
- [18] A. Vonk-Noordegraaf, P. W. A. Kunst, A. Janse, J. T. Marcus, P. E. Postmus, T. J. C. Faes and P. M. J. M. de Vries, **Pulmonary perfusion measured by means of electrical impedance tomography**, *Physiological Measurement*, **19** (1998), 263. <http://stacks.iop.org/0967-3334/19/i=2/a=013>.

Received June 2024; revised September 2024; early access September 2024.